tude measurement stability is monitored by measuring a fixed time delay line within the altimeter system. The bias of this calibration has been consistently less than 20 cm over a 4-month period. Finally, to establish a more absolute comparison with geoids measured with other techniques, a constant tropospheric refraction correction of 2.79 m was subtracted from each altitude measurement.

The Skylab orbital positions were estimated by an orbit determination program with the use of unified S-band (USB) range and range rate tracking data obtained from the Goddard Space Flight Center. Because of the large drag effect on the spacecraft and the thrusting used for spacecraft maneuvers, the lengths of the orbital solutions were minimized, resulting in an uncertainty in the calculated orbital height of about 25 m.

A major preliminary result of an altimeter-sensed ocean profile is shown in Fig. 1. Data were acquired from EREP pass 4, SL-2, on 4 June 1973, when Skylab was passing from a point off the east coast of South Carolina to a point just south of Puerto Rico, as shown in Fig. 1A. The difference between the altitude calculated to the ellipsoid ($a = 6{,}378{,}155$ m, $f = 1/298.255$, where a is the length of the semimajor axis and f is the flattening of the ellipsoid) and the altitude measured by the altimeter to the ocean surface is shown in Fig. 1B. A bottom topography profile along the subsatellite trace, derived from Pratt (*3*), is shown in Fig. 1B. Note the 4-m drop in the ocean surface profile over the Blake Escarpment, the low-frequency rise at abyssal plain area, and the 15-m depression in the ocean surface over the Puerto Rico Trench, a 100-km wavelength feature. The relative disagreement of the minima of the two profiles over the trench can be explained in terms of local gravity conditions. Bowin *et al.* (*4*) observed a similar disagreement over the trench minima between the free-air anomaly and water depth measurements. Moreover, the difference in slope between the north and south flanks of the trench are clearly evident in the altitude residuals. Von Arx (*5*) and Stanley *et al.* (*6*), using independent techniques, have estimated ocean profile depressions of 17.5 and 22.5 m, respectively, across different sections of the trench.

Figure 2 depicts a similar comparison of data from EREP pass 11, SL-3, taken on 2 September 1973, just off the east coast of Brazil over the South Atlantic. The ground track for the pass is shown in Fig. 2A. The altimeter measurement residuals from the USB-determined orbit in Fig. 2B show an interesting anomaly in the ocean surface profile. Comparing the anomaly with the ocean bottom topography derived from Uchupi (*7*), also presented in Fig. 2B, we see a distinct correlation of the second seamount with the high-frequency signature from the altitude residuals. The first seamount does not have as great an effect on the sea surface because it has less mass and is not part of a seamount chain as is the second seamount. In addition to these specific results, the Mid-Atlantic Ridge, the Cape Verde Islands, the Mid-American Trench, and the Flemish Cap have each had a detectable influence on the altimeter-sensed ocean surface topography.

In conclusion, we feel that the Skylab altimeter has significantly demonstrated an ability to detect and map even short-wavelength undulations in the ocean geoid. In addition, these short-wavelength undulations are often highly correlated with major ocean bottom topography. Therefore, the potential of satellite altimeters for charting mass density distributions and for contributing to the understanding of the earth's geological structure can easily be recognized.

C. D. LEITAO
J. T. MCGOOGAN
National Aeronautics and Space Administration, Wallops Flight Center, Wallops Island, Virginia 23337

References and Notes

1. J. T. McGoogan, paper presented at the Institute of Electrical and Electronics Engineers International Convention and Exposition, New York, March 1974.
2. J. T. McGoogan, L. S. Miller, G. S. Brown, G. S. Hayne, *Proc. Inst. Elec. Electron. Eng.* **62**, 793 (1974).
3. R. M. Pratt, *Atlantic Continental Shelf and Slope of the United States: Physiography and Sediments of the Deep-Sea Basin* (Government Printing Office, Washington, D.C., 1968), plate 1.
4. C. O. Bowin, R. Bernstein, E. D. Ungar, J. R. Madigan, *Inst. Elec. Electron. Eng. Trans. Geosci. Electron.* **GE-5**, 2 (1967).
5. W. S. von Arx, *Science* **154**, 1651 (1966).
6. H. R. Stanley, C. F. Martin, N. A. Roy, A. G. Mourad, paper presented at 15th General Assembly of the International Union of Geodesy and Geophysics, Moscow, August 1971.
7. E. Uchupi, "Bathymetric atlas of the Atlantic, Caribbean, and Gulf of Mexico" (unpublished manuscript, Reference No. 71-72, Woods Hole Oceanographic Institution, Woods Hole, Mass., December 1971).
8. We thank W. T. Wells for assistance in the orbital analysis, T. D. Sommers and V. E. Hopkins for programming support, W. Speidel for technical support, and the referees for their helpful suggestions.

15 July 1974; revised 30 September 1974

Electron Imaging of Pyrrhotite Superstructures

Abstract. *Natural pyrrhotites, when studied by high resolution electron microscopy, yield crystallographic information on a unit cell scale. Structural heterogeneity is prominent. The many reported superstructures are interpretable through an antiphase model. The 5C pyrrhotite superstructure results from an ordered sequence of antiphase domains while the higher temperature* NC *type results from a disordered sequence.*

Pyrrhotite, $Fe_{1-x}S$, is a geologically interesting, industrially important, and crystallographically complex mineral. It has commonly been used as a type example of nonstoichiometry. At low temperatures, however, it appears to consist of a series of chemically and structurally discrete phases related by superstructuring. In spite of extensive studies, a number of problems persist: (i) there is confusion regarding the exact number and stabilities of its many reported superstructures, (ii) detailed information on the mechanism of superstructure formation is lacking, and (iii) there is apparently a direct relation between the length of the superstructure in the *c*-direction and the composition (*1*), but the nature of this relation is not yet clear (*2*).

Detailed structural information on a unit cell level has been obtained for silicate minerals by using high resolution electron microscopy (*3, 4*). It was thought that electron microscopy would provide information pertinent to the problems of pyrrhotite superstructuring beyond that obtainable by x-ray techniques. A successful study of pyrrhotite would also indicate the applicability of high resolution electron microscopy to structure problems of other sulfides.

Cell dimensions of pyrrhotite super-

structures can be considered multiples of a hexagonal subcell with $a = 3.45$ Å $\equiv A$ and $c \sim 5.8$ Å $\equiv C$ (*5*). A large assortment of integral multiples of *C*, most also having a 2*A* superstructure, have been reported: 2*C* (*6*), 4*C* (*7, 8*), 5*C* (*9*), 11*C* (*9*), 6*C* (*9*), and 7*C* (*10*). Superstructures with non-integral multiples have also been reported: *NC* type with $N = 3.0$ to 4.0 (*11*), *MC* type with $M = 3.0$ to 4.0 (*12*), and *NA*-3*C* type with $N = 40$ to 90 (*9*). Determinations of the pyrrhotite phase diagram have been attempted, but with conflicting results (*10, 12*).

Previously described experimental procedures (*3*) were used with two additional precautions: (i) since oxidation alters the composition and structure of pyrrhotite (*13*), samples are ground under acetone and subsequently stored under acetone or vacuum; and (ii) care is taken to minimize structural changes caused by electron beam bombardment by selecting crystals that are small, thin, and have a large surface contact with the supporting film. Regardless of crystal selection, local temperatures in the specimen are not precisely known during electron microscopy, and some phase transformations are observed (*14*). However, structure changes are usually not observed in crystals meeting the above criteria.

Bright field and dark field modes of the electron microscope were used. The interpretation of both kinds of images has been recently reviewed (*15, 16*) and applied to pyrrhotite images (*17*). High resolution bright field images correspond directly with structure for thin (~ 100 Å) crystals at optimum instrument defocus (*18*); bright field photographs used in this study were taken under these conditions.

Dark field electron micrographs, for the most part, do not have a simple relationship to structure. However, dark field images of edges of thin crystals at an underfocus of ~ 300 Å (*19*) can correspond to structure (*15*). Direct interpretation of dark field micrographs in this study is made possible by the fact that the subcell structure of pyrrhotite is well known. If this subcell structure is correctly imaged in a given photograph, then any superstructure present will also be imaged correctly.

To facilitate dispersion on the electron microscope grid, relatively non-

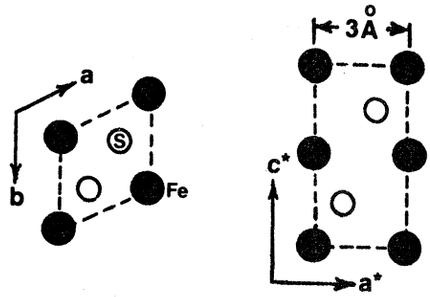

Fig. 1. The pyrrhotite structure as viewed down *c* (left) and *b* (right).

magnetic specimens (*20*) were studied. X-ray powder patterns indicate that the samples are apparently hexagonal single phases. Electron diffraction, however, shows that all are, in fact, polyphasic. Predominantly 5*C* and *NC* electron diffraction patterns were obtained, but many other intimately associated, coexisting *c*-superstructure spacings were also observed. For example, a ½-mm pyrrhotite crystal from Franklin, New Jersey (Arizona State University specimen number 88) typically contains superstructure spacings corresponding to 5*C*, 4*C*, *NC* with $N = 4.0$ to 5.5, 10*C*, 7*C*, and 28*C* (listed in order of decreasing abundance). The 10*C* and 28*C* spacings have not previously been reported. The average composition of the sample, $Fe_{.91 \pm .01}S$ [determined from the d_{120} spacing method of Arnold (*21*)] corresponds to that of the 11*C* type of Nakazawa and Morimoto (*12*). Heterogeneity on such a scale (*22*) raises serious questions regarding the use of pyrrhotite for geothermometry and geobarometry (*23*). In fact, any calculation assuming equilibrium in pyrrhotite may be in error.

Figure 1 shows the pyrrhotite structure. The drawing at the left illustrates a projection of structure in the same direction from which the electron micrographs in this report are taken. In the dark field electron micrograph, Fig. 2, projections of Fe atoms appear as bright dots (compare Fig. 1). Sulfur atoms do not appear in the image; apparently they present a broader and less intense potential projection than Fe atoms.

In the upper left of Fig. 2, bright rows of dots alternate in the *c**-direction with dim rows of dots. This modulation in intensity results from differences in Fe site population density (*24*). This observation that Fe-rich layers alternate in the *c**-direction with relatively vacancy-rich layers is consistent with the type of model proposed by Bertaut (*25*) and confirmed by Tokonami *et al.* (*26*) for 4*C* pyrrhotite, and extended to artificial 3*C* pyrrhotite by Fleet (*27*).

In the center of Fig. 2, the first intensity modulation is joined by a modulation perpendicular to *c**, which results from a periodicity of twice the *a*-length: a 2*A* superstructure. Iron-rich sites alternate with more vacancy-rich sites, again consistent with earlier models. In this photograph, vacancy-rich sites are offset perpendicular to the *c**-direction by one subcell width between vacancy-rich layers.

Structures similar to the image in Fig. 3a (with oriented diffraction pattern Fig. 3b) are common in pyrrhotites. The marked area is schematically illustrated in Fig. 3c, with sites interpreted as nearly filled with Fe atoms marked *f*, and sites relatively depleted in Fe atoms left blank.

By marking columns in Fig. 3c as *1* and *2*, a further simplification can be made: horizontal rows with blanks occurring in columns of type 1 are designated as *1* in Fig. 3d, and horizontal rows with blanks in the columns of type 2 are designated as *2*. Horizontal rows in which all sites are nearly full are designated as *F*. Figure 3d is then a sequence of stacking of Fe layers along *c** (*28*), in this example (*F1F2F2F1F2F2F1F1F2F1F*).

The most striking thing about such sequences is their apparent randomness. The *c*-superstructure, so evident in the diffraction pattern, is not obvious in the image. Periodicities in images of pyrrhotite can be recognized by using a series of antiphase models that closely approximate the structures seen in electron micrographs of real crystals. In each model, the crystal is considered to consist of a series of platelike antiphase domains, stacked in the *c**-direction, and extending more or less indefinitely perpendicular to *c**. For example, in a stacking series such as Fig. 3d if the sequence (*F1F1F1* . . .) is defined as the normal phase, then (*F2F2F2* . . .) is the antiphase. Alternatively, the normal phase could be defined as (*F1F2F1F2F1* . . .).

Minagawa (*29*) has derived an equation for calculation of superstructure x-ray diffraction intensities resulting from antiphase domains in a disordered array. The calculated intensities and

positions of diffraction maxima depend on the thicknesses of the domains (relative to the subcell) and the degree of disorder in their sequence. Calculations of this sort can be compared to electron diffraction data, keeping possible dynamical complications in mind (*30*). In practice, the domain thicknesses (in numbers of subcells) and sequences are determined from structure images, the degree of disorder in the sequences is calculated, and finally the superstructure intensities are computed from the Minagawa equation.

The limitation of the equation is that only periodicities resulting from adjacent domains are considered. In the case of pyrrhotite, this results in different calculated spacings depending on how the normal phase is defined. The two models with normal phases defined as (*F1F1F1* . . .) and (*F1F2-F1F2* . . .) seem to produce most periodicities seen in pyrrhotite. A composite diffraction pattern, consisting of the sum of intensities calculated from both models, can reproduce observed pyrrhotite diffraction patterns.

In the bright field structure image of 5*C* pyrrhotite (Fig. 4a), 6-Å interference fringes parallel to c^* indicate the 2*A* superstructure. Bright dots in this photograph correspond to vacancy-rich sites. The corresponding diffraction pattern is shown in Fig. 4b. The obvious feature of the image is the repeating sequence (*F1F1F2F2F2F1-F1F2F2F2* . . .). The observed pattern, schematically illustrated in Fig. 4c, agrees well with the calculation (Fig. 4d) for the model with normal phase defined as (*F1F1* . . .), although the observed intensities for the middle two superstructure spots are greater than the calculated ones, possibly because of dynamic scattering. Peaks corresponding to the model with normal phase of (*F1F2F1* . . .) are apparently too weak to be observed.

The (*F1F1F2F2F2F1F1F2F2F2* . . .) sequence produces a 5*C* superstructure spacing, but any other five-subcell sequence will give a 5*C* spacing as well. More significantly in the case of pyrrhotite, calculations show that a 5*C* spacing with the middle two spots attenuated or absent (such as we observe for nonintegral pyrrhotite) will result from a combination of equal numbers of antiphase domains two and three subcells thick in a disordered sequence. We think that the ordered sequence of domains seen is representative of the

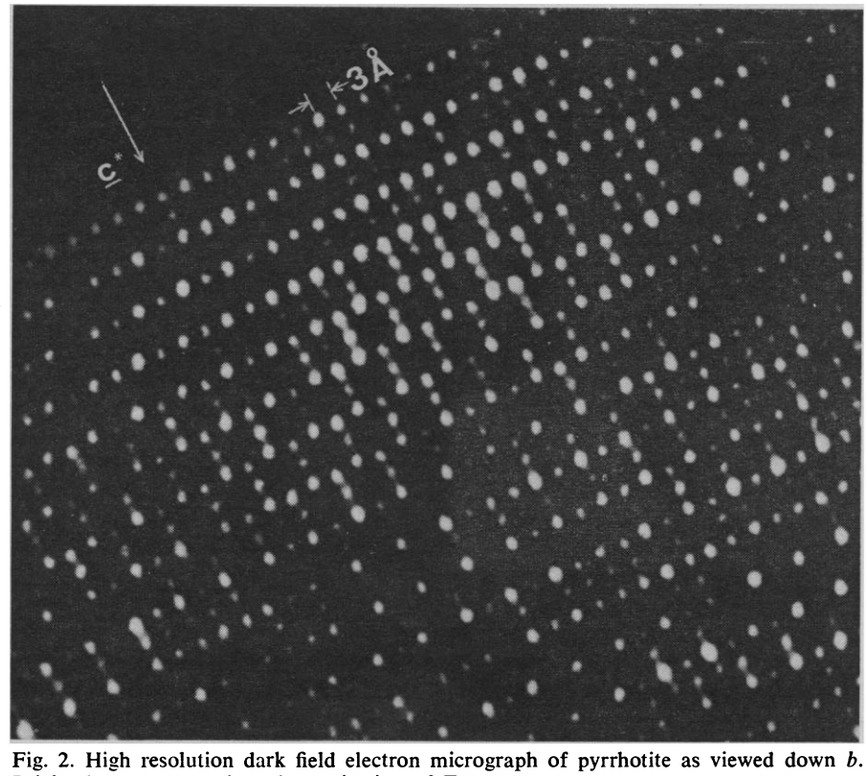

Fig. 2. High resolution dark field electron micrograph of pyrrhotite as viewed down *b*. Bright dots correspond to the projection of Fe atoms.

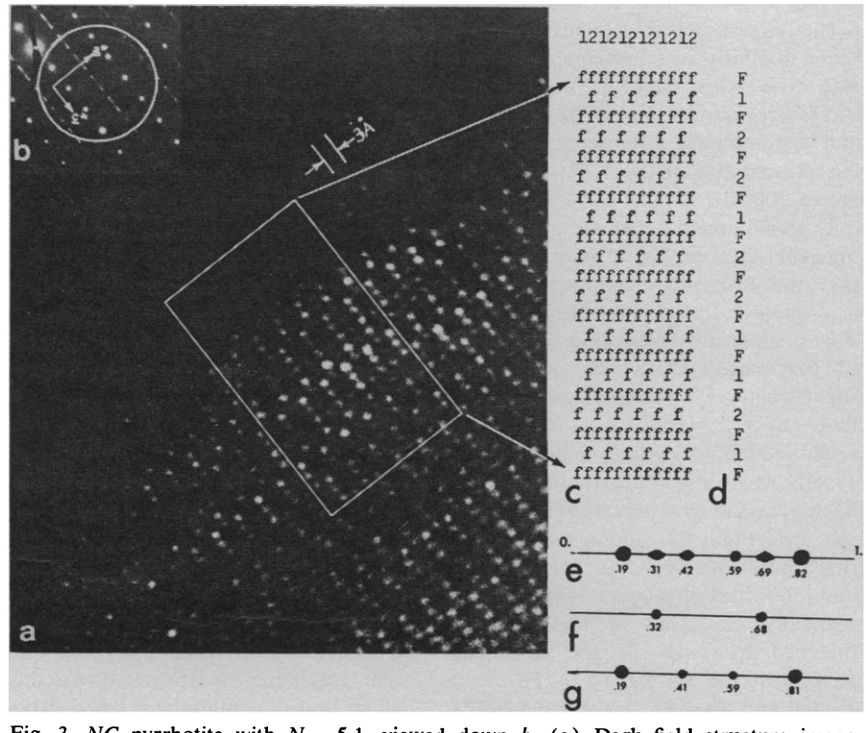

Fig. 3. *NC* pyrrhotite with $N = 5.1$, viewed down *b*. (a) Dark field structure image. Bright dots correspond to the projection of Fe atoms along *b*. (b) Oriented diffraction pattern of (a). The marked circle indicates the placement of the objective aperture. (c) Schematic diagram of the marked rectangle in (a) (see text for description). (d) Sequence of Fe layer stacking shown by (a) and (c) (see text for description). (e) Schematic diagram of observed 10*l* reciprocal lattice row in (b). Numbers indicate relative positions of peaks. (f) The 10*l* reciprocal lattice row calculated from the antiphase model with normal phase sequence = (*F1F1F1* . . .). (g) The 10*l* reciprocal lattice row calculated from the antiphase model with normal phase sequence = (*F1F2F1* . . .).

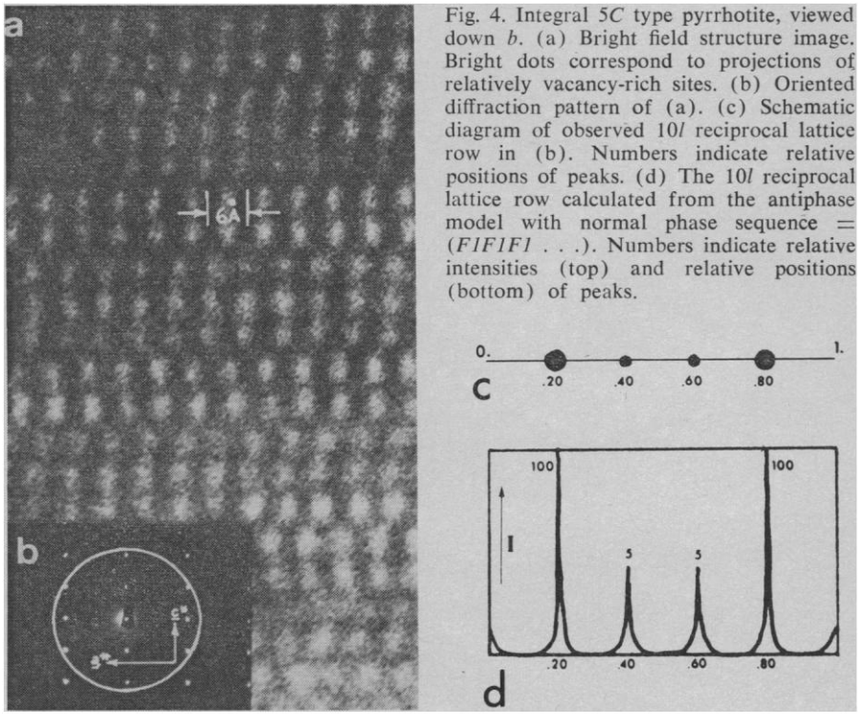

Fig. 4. Integral 5*C* type pyrrhotite, viewed down *b*. (a) Bright field structure image. Bright dots correspond to projections of relatively vacancy-rich sites. (b) Oriented diffraction pattern of (a). (c) Schematic diagram of observed 10*l* reciprocal lattice row in (b). Numbers indicate relative positions of peaks. (d) The 10*l* reciprocal lattice row calculated from the antiphase model with normal phase sequence = (*F1F1F1* . . .). Numbers indicate relative intensities (top) and relative positions (bottom) of peaks.

integral *5C* type pyrrhotite reported as stable below 100°C (*9*), while a partially disordered sequence of the same domains is representative of an *NC* type with $N = 5.0$, reported as stable between 100° and 200°C (*12*), and a completely disordered sequence is representative of the *MC* type, stable above 200°C (*12*).

If two domain sizes are present in unequal numbers in a disordered array, the Minagawa equation predicts a nonintegral superstructure spacing. This is especially interesting in the case of pyrrhotite, which has nonintegral superstructures at temperatures greater than 100°C.

A disordered array of domains is exactly what is seen in structure images having nonintegral electron diffraction spacings. Figure 3a shows an *NC* type pyrrhotite with $N = 5.1$. All positions and intensities of observed peaks (schematically illustrated in Fig. 3e) are matched by those of the calculated peaks [Fig. 3f for the (*F1F1F1* . . .) model and Fig. 3g for the (*F1F2F1* . . .) model], illustrating the production of large spacings ($\sim 10C$) from a disordered sequence of antiphase domains. Other examples seen in the study present convincing evidence that the pyrrhotite nonintegral superstructures result in large part from disordered stacking of antiphase domains.

The disordered stacking of different types of Fe layers along c^* that is observed in structure images helps to explain some of the problems of the pyrrhotite structures. The many possible permutations of stacking sequences result in many superstructures within a small compositional range. In fact, all the reported nonintegral values of *c*-superstructure spacing (*9, 11, 12*) can be calculated by hypothesizing combinations of antiphase domains one, two, and three subcells thick. Strict confirmation of whether antiphase behavior is indeed responsible for all superstructure spacings in pyrrhotite requires (i) extension of the calculations to include domains of at least three different sizes and to recognize periodicities resulting from more than pairs of domains and (ii) study of structure images of crystals having compositions from the entire pyrrhotite range. The imaging of rows of metal atoms in pyrrhotite suggests that high resolution electron microscopy will be useful in studying the fine structure of other sulfides as well.

LARRY PIERCE
Department of Chemistry,
Arizona State University,
Tempe 85281

PETER R. BUSECK
Departments of Geology and *Chemistry,*
Arizona State University

References and Notes

1. M. Rieder, *Vestn. Ustred. Ustavu Geol.* **48**, 35 (1973).
2. M. E. Fleet, *ibid.*, p. 311.
3. P. R. Buseck and S. Iijima, *Am. Mineral.* **59**, 1 (1974).
4. S. Iijima, J. M. Cowley, G. Donnay, *Tschermaks Mineral. Petrogr. Mitt.* **20**, 216 (1973).
5. H. Haraldsen, *Z. Anorg. Allg. Chem.* **246**, 169 (1941).
6. G. Hägg and I. Sucksdorff, *Z. Phys. Chem. Abt. B* **22**, 444 (1933).
7. M. J. Buerger, *Am. Mineral.* **32**, 411 (1947).
8. E. F. Bertaut, *C. R. Hebd. Seances Acad. Sci.* **234**, 1295 (1952).
9. N. Morimoto, H. Nakazawa, K. Nishiguchi, M. Tokanami, *Science* **168**, 964 (1970).
10. G. A. Desborough and R. H. Carpenter, *Econ. Geol.* **60**, 1431 (1965).
11. N. Morimoto and H. Nakazawa, *Science* **161**, 577 (1968).
12. H. Nakazawa and N. Morimoto, *Proc. Jap. Acad.* **46**, 678 (1970).
13. P. R. Buseck, *Am. Mineral.* **48**, 911 (1964).
14. Spacings between superstructure spots in the c^*-direction were not observed to change, but intensities changed markedly in thick crystals. Calculations show that these changes may be due to the introduction of disorder in the crystal, and perhaps correspond to a transformation from the integral *5C* type to *NC* with $N = 5.0$. With electron irradiation the *NA* type superstructure, not initially present, was seen to form with $N \sim 25$.
15. J. M. Cowley, *Acta Crystallogr. Sect. A* **29**, 529 (1973).
16. ———, in *Principles and Techniques of Electron Microscopy*, M. A. Hayat, Ed. (Van Nostrand Reinhold, New York, in press).
17. L. Pierce and P. R. Buseck, in *Application of Electronmicroscopy to Minerals*, H. R. Wenk, Ed. (Springer-Verlag, Heidelberg, Germany, in press).
18. We used a 900-Å underfocus for a 100-kv accelerating potential and a spherical aberration constant of 1.8 mm. J. M. Cowley and S. Iijima, *Z. Naturforsch. A* **27**, 445 (1972).
19. In practice, precise determination of underfocus in the dark field mode is extremely difficult. The best photographs of a "through focus series" are used.
20. The specimens were from Franklin, N.J. (Arizona State University Geology Collection No. 88 and Paterson Museum, Paterson, N.J., No. F102); Hillburn, N.Y. (Paterson Museum No. G-1467); and Scarsdale, N.Y. (Paterson Museum No. G-1469).
21. R. G. Arnold, *Econ. Geol.* **57**, 72 (1962).
22. In this regard, pyrrhotite resembles the Ca-poor pyroxenes as they also display similar intergrowths on a unit cell level. S. Iijima and P. R. Buseck, *Am. Mineral.*, in press; P. R. Buseck and S. Iijima, *ibid.*, in press.
23. L. A. Clark, *Econ. Geol.* **60**, 792 (1965); S. D. Scott and H. L. Barnes, *ibid.* **66**, 653 (1971).
24. Displacements of Fe atoms from their idealized sites could conceivably produce similar intensity attenuation. Such displacements have been reported (*25, 26*). However, periodic displacements in pyrrhotite occur in response to periodic vacancies, and Fe vacancies would be expected to produce greater attentuation than Fe displacements. The major fluctuations in site intensity in the photograph are undoubtedly due to vacancy distribution.
25. E. F. Bertaut, *Acta Crystallogr.* **6**, 557 (1953).
26. M. Tokonami, K. Nishiguchi, N. Morimoto, *Am. Mineral.* **57**, 1066 (1972).
27. M. E. Fleet, *Acta Crystallogr. Sect. B* **27**, 1864 (1971).
28. Structure images are two-dimensional projections. Unfortunately, three-dimensional stacking sequences of pyrrhotites are not obtainable from the photographs in this report.
29. T. Minagawa, *Acta Crystallogr. Sect. A* **28**, 308 (1972).
30. J. M. Cowley, in *Proceedings of the Electron Microscopy Society of America, 32nd Annual Meeting*, C. J. Arceneaux, Ed. (Claitor's, Baton Rouge, La., in press).
31. We thank J. M. Cowley, R. Von Dreele, J. Armstrong, and E. Holdsworth for their helpful comments and T. M. Peters, director of the Paterson Museum, for specimens. Financial support was provided by NSF grant GA25701.

21 October 1974